Journal of Biomedical Optics

SPIEDigitalLibrary.org/jbo

Concurrent multiscale imaging with magnetic resonance imaging and optical coherence tomography

Chia-Pin Liang
Bo Yang
Il Kyoon Kim
George Makris
Jaydev P. Desai
Rao P. Gullapalli
Yu Chen

SPIE

Concurrent multiscale imaging with magnetic resonance imaging and optical coherence tomography

Chia-Pin Liang,[a] Bo Yang,[b] Il Kyoon Kim,[a] George Makris,[c] Jaydev P. Desai,[b] Rao P. Gullapalli,[c] and Yu Chen[a]
[a]University of Maryland, Fischell Department of Bioengineering, College Park, Maryland 20742
[b]University of Maryland, Department of Mechanical Engineering, College Park, Maryland 20742
[c]University of Maryland School of Medicine, Department of Diagnostic Radiology and Nuclear Medicine, Baltimore, Maryland 21201

Abstract. We develop a novel platform based on a tele-operated robot to perform high-resolution optical coherence tomography (OCT) imaging under continuous large field-of-view magnetic resonance imaging (MRI) guidance. Intra-operative MRI (iMRI) is a promising guidance tool for high-precision surgery, but it may not have sufficient resolution or contrast to visualize certain small targets. To address these limitations, we develop an MRI-compatible OCT needle probe, which is capable of providing microscale tissue architecture in conjunction with macroscale MRI tissue morphology in real time. Coregistered MRI/OCT images on *ex vivo* chicken breast and human brain tissues demonstrate that the complementary imaging scales and contrast mechanisms have great potential to improve the efficiency and the accuracy of iMRI procedure. [DOI: 10.1117/1.JBO.18.4.046015]

Keywords: optical coherence tomography; magnetic resonance imaging; multimodal imaging.

Paper 12830LR received Jan. 2, 2013; revised manuscript received Mar. 7, 2013; accepted for publication Mar. 19, 2013; published online Apr. 22, 2013; corrected Apr. 23, 2013.

The superior tissue contrast and versatile imaging protocols of intra-operative magnetic resonance imaging (iMRI) make it a promising guidance tool for various surgeries.[1–3] MRI-compatible robotic systems that can operate inside the MRI bore with near real-time MRI guidance have been developed.[4–6] These systems are promising, but their targeting capability is still limited by the resolution of MRI. Moreover, artifacts of the surgical tools (such as metallic electrode or biopsy needle) obscure the important region of interest and make it difficult to achieve submillimeter accuracy. In this paper, we integrate an optical coherence tomography (OCT) probe with an MRI-compatible robot and use the microscopic OCT information to deliver the biopsy needle with unprecedented accuracy. The combination of macroscale MRI morphology and microscale OCT architecture in a coregistered manner paves a new avenue to iMRI interventions that require submillimeter precision.

Figure 1(a) shows the integrated MRI/OCT imaging system, which includes an MRI-compatible robot.[5] To work within a 3T MRI (Siemens), we actuate the robot by a pneumatic cylinder. By pressurizing or depressurizing the air chambers in the pneumatic cylinder using a pneumatic directional control valve (MPYE-5-1, Festo) connected to an air compressor, we can move the needle forward or backward. The MRI-incompatible pressure control units are placed outside the MRI room and are connected to the robot through long plastic tubes. The position of the needle is recorded by an encoder with 12.7-μm resolution for feedback control. The smallest step size of the pneumatic robot is 1 mm, and the response time for 1-mm displacement is 0.2 s. The OCT system uses a swept-source laser centered at 1325 nm with a spectrum bandwidth of 100 nm (SL1325-P16, Thorlabs). The wavelength-swept frequency is 16 kHz with 12-mW output power. The OCT system[7] sitting outside the MRI room is connected to a side-viewing OCT probe (Imagewire, St. Jude Medical) through an 8-mm-long single-mode fiber (SMF). The side-viewing probe consists of a SMF for light transmission, a gradient index (GRIN) multimode fiber for light focusing, and a micro-mirror for beam deflection [Fig. 1(b)]. The OCT probe (outer diameter = 0.23 mm) is placed in a 16-gauge (outer diameter = 1.7 mm) titanium biopsy needle (*In vivo*). We create a side window on the needle to allow the laser beam to reach the sample and encapsulate the window with transparent heat shrink tubing (HST) to prevent tissue collection [Fig. 1(c)]. The measured working distance from the outer surface of the needle is 0.2 mm. The HST deteriorates the transverse resolution from 20 to 30 μm, whereas the axial resolution remains 15 μm. We minimize the sensitivity drop introduced by the HST to 1–2 dB by filling the needle with water for index matching. The OCT probe is linearly actuated along the long axis of the needle by an MRI-compatible lead zirconatetitanate (PZT) actuator (Piezo Systems) attached at the proximal end. We use only the information from pull-back direction, since it is difficult to insert a flexible fiber linearly from a distal site. The PZT actuator and the OCT needle probe are moved in tandem, driven by the pneumatic actuator.

We use a custom-made phantom to coregister the MRI and OCT images. A plastic sheet (thickness = 1 mm) with holes that are large enough for the OCT needle to pass through is immersed in a water-filled container. The OCT needle goes through a hole on the phantom until the side window lines up with the plastic sheet so that the reflection from the plastic sheet is visible in OCT [Fig. 2(c)]. The OCT laser beam is pointed downward (i.e., the plane containing the needle central axis and OCT beam is normal to the MRI table). In MRI images [Fig. 2(a) and 2(b)], the plastic sheet (white arrows), the needle,

Address all correspondence to: Yu Chen, University of Maryland, 2218 Jeong H. Kim Building, College Park, Maryland 20742. Tel: +301.405.3439; Fax: +301.405.9953; E-mail: yuchen@umd.edu

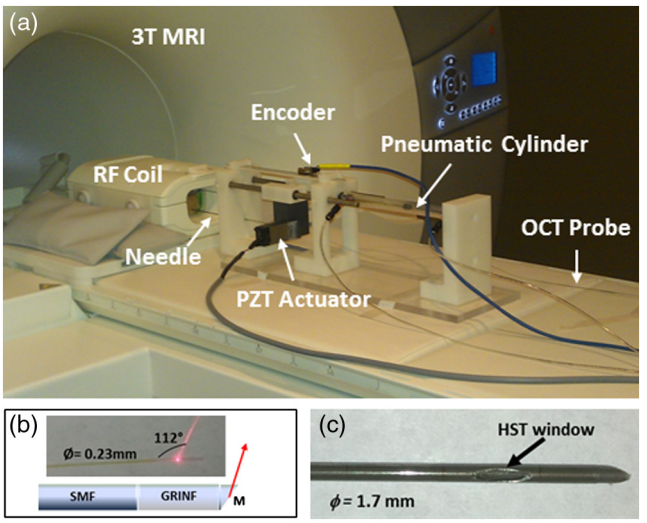

Fig. 1 (a) Combined MRI/OCT imaging system. (b) Side-viewing OCT probe consisting of single-mode fiber (SMF), gradient index multimode fiber (GRINF), and micro-mirror (M). (c) MRI-compatible titanium needle probe for OCT imaging, with side window covered by transparent heat shrink tubing (HST).

and the artifacts from the needle tip and the side window (red arrows) are clearly visible. Because the OCT imaging window has been aligned with the plastic sheet, the sheet in the MRI images indicates the location of the OCT window. Therefore, we can locate the OCT window in the MRI image and measure the distance from the OCT window to the needle tip. Although the encoder can track the needle position with 12.7-μm resolution, the accuracy of coregistration cannot be better than the resolution of MRI (~1 mm).

We demonstrate the multiscale imaging on chicken breast tissue *ex vivo*. We place the chicken breast in a wrist coil for MRI. High-resolution T2 MRI (4 min/frame) images are acquired before needle insertion to plan the trajectory and after needle insertion to verify the final location. Although high-resolution T2 MRI can resolve the millimeter-scale structures [Fig. 3(a)], its long image acquisition time makes it impossible for real-time guidance. Figure 3(b) to 3(d) shows the enlarged MRI images of the area indicated in Fig. 3(a); panels 3(e)–3(g) are the corresponding OCT images. At position B, the needle is in a homogeneous muscle tissue, and its corresponding OCT image [Fig. 3(e)] also shows similar feature. At position C, the needle is very close to fibrous connective tissues. The corresponding OCT image [Fig. 3(f)] shows the same structure with few finer fibers beneath it. At position D, the OCT image reveals fine connective tissues within muscular tissues. Figure 3(h) (Video 1) shows the concurrent dynamic MRI and OCT during needle insertion. Low-resolution dynamic MRI (1 frame/s) provides the general needle location and real-time OCT (15 frame/s) reveals the microstructures surrounding the needle. Therefore, the operator can estimate in real time the distance to the target from the dynamic MRI image and decide whether the needle reaches the target based on the OCT tissue architecture. The nonlinear motion is obvious while the needle is inserted into the chicken breast (Video 1). Speckle cross-correlation[8,9] could be applied in future studies to improve the uniformity.

We image an *ex vivo* human basal ganglia to demonstrate the potential of MRI/OCT for neurosurgery guidance. iMRI has been applied to many stereotactic neurosurgeries, including brain tumor biopsy,[10] catheterization,[11] and deep brain stimulation.[3,12] However, the resolution and the contrast of MRI are not high enough to detect certain target nuclei in basal ganglia.[13] On the other hand, OCT can locate these nuclei in human brain *ex vivo*[14] and rat brain *in vivo*.[15] We place a slab of frozen human brain tissue containing basal ganglia in a gelatin holder filled with saline at room temperature and wait until it is completely thawed. Then, we acquire preoperative T2 MRI images to plan the trajectory. We monitor the advancement of the needle by dynamic MRI and OCT in real time [Fig. 4(e), Video 2]. In OCT video, we can easily identify the boundary between the gray matter (GM) and the white matter (WM), whereas most of structures are occult in the dynamic MRI video. Figure 4(a) shows a photo of the brain tissue. In the high-resolution MRI image [Fig. 4(b)], the transitions between the GM nucleus, putamen (PUT, white on T2 image) and its surrounding WM bundles, white matter lamina (WL), and internal capsule (IC)

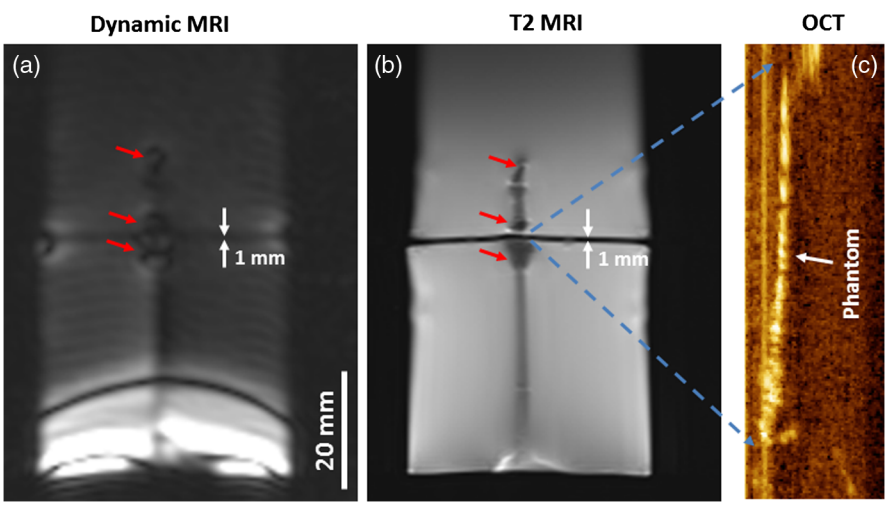

Fig. 2 Coregistration of MRI and OCT images using a custom-made phantom. Dynamic MRI (a) and high-resolution T2 MRI (b) images of OCT needle and plastic sheet phantom (indicated by white arrows). The artifacts from sharp edges on the needle tip and the side window are indicated by red arrows. (c) Concurrent OCT image of plastic sheet phantom. OCT FOV covers the entire 1-mm thickness of the phantom for coregistration of OCT images with low-resolution dynamic MRI and high-resolution T2 MRI images.

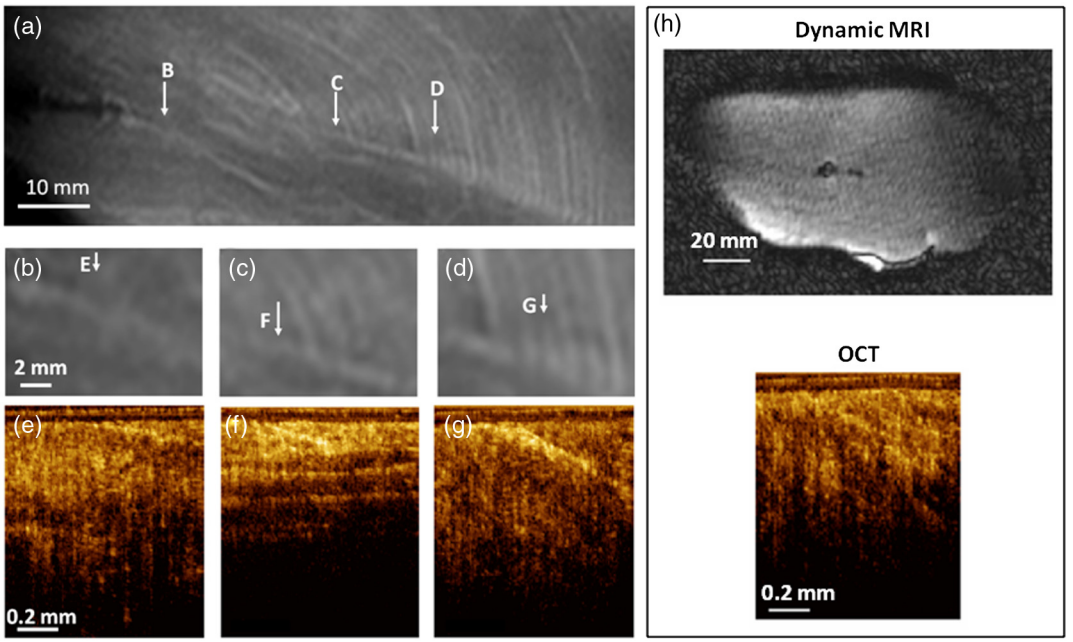

Fig. 3 Coregistered MRI/OCT images of chicken breast tissues *ex vivo*. (a) High-resolution T2 MRI image; arrows B, C, and D indicate the positions of corresponding enlarged MRI images shown in (b)–(d) and OCT images shown in (e)–(g). (H) Concurrent dynamic MRI and OCT imaging of chicken breast tissue during needle insertion. (Video 1, MOV, 60 MB) [URL: http://dx.doi.org/10.1117/1.JBO.18.4.046015.1].

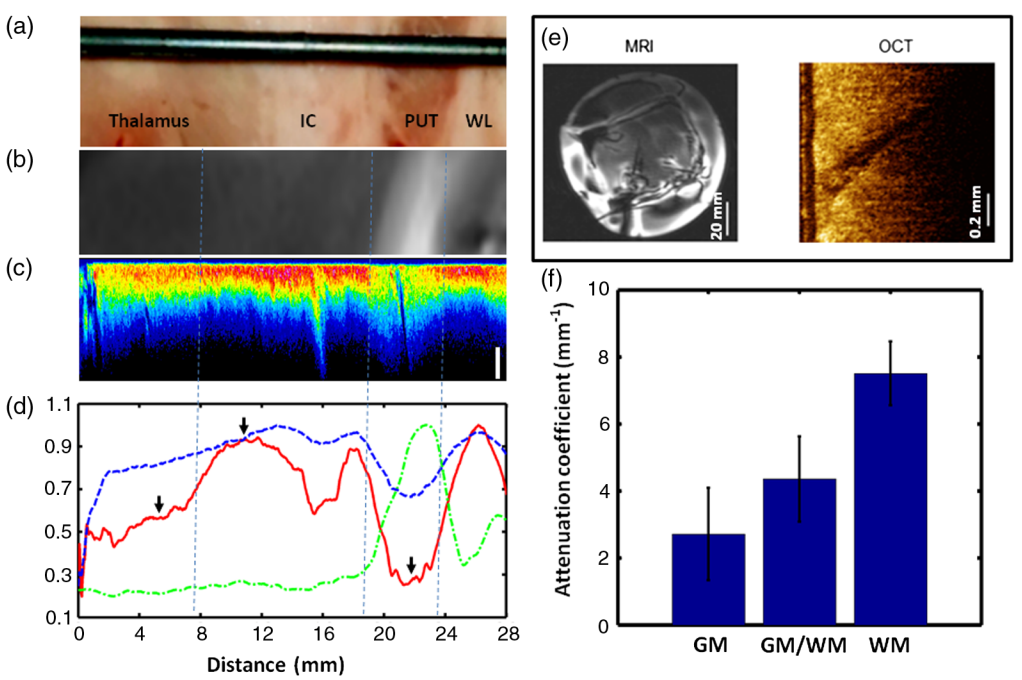

Fig. 4 Coregistered MRI/OCT images of human basal ganglia *ex vivo*. (a) Human brain tissue containing basal ganglia. Different tissues types are visible, including white matter lamina (WL), putamen (PUT), internal capsule (IC), and thalamus. The OCT needle probe is sitting on top of the tissue, indicating the insertion track (the actual insertion track is beneath the tissue surface). (b) T2 MRI image of the brain slice. (c) Full-tack OCT with coregistered lateral position with MRI. The axial dimension is expanded for better visualization. The scale bar for the axial dimension is 0.5 mm. (d) Plot of normalized MRI intensity (green), normalized OCT backscattering intensity (blue), and normalized OCT attenuation coefficient (red). (e) Concurrent dynamic MRI and OCT imaging of human brain tissue during needle insertion (Video 2, MOV, 95 MB) [URL: http://dx.doi.org/10.1117/1.JBO.18.4.046015.2]. (f) Attenuation coefficient of GM (PUT), GM/WM mixture (thalamus), and WM (IC). The *P* values between data sets are <0.0001.

(dark on T2 image) are clearly visible. We reconstruct a full-track OCT image [Fig. 4(c)] from the OCT video and correlate it with the large-scale MRI morphology. From each frame of the OCT video, we select a band of A-lines with 66.67-μm width (1 mm/s sampling rate, same as the needle insertion speed) from the same location. Then, we stitch these bands together to form Fig. 4(c). We align the pre-operative MRI to the intra-operative OCT by matching them to the dynamic MRI images. The accuracy of the alignment is limited by the resolution of the dynamic MRI image, which is 2 mm. In Fig. 4(d), we plot the normalized MRI intensity (green line), normalized OCT backscattering intensity (blue line), and normalized attenuation coefficient (red line). The normalized OCT attenuation coefficient and OCT backscattering in Fig. 4(e) are smoothed for better visualization by a moving average filter with 2.35 mm average width. In the full-track OCT image, the transitions between PUT and its surrounding WM bundles (WL and IC) are obvious and well correlated with the MRI image. The full-track OCT shows that the GM nucleus (PUT) has lower backscattering intensity, deeper penetration depth, and thus smaller attenuation coefficient [Fig. 4(d)], whereas myelinated WM tracks have higher backscattering intensity, shallower penetration depth, and larger attenuation coefficient. This result agrees well with previous study.[16] In addition, the transition from IC to thalamus is not visible in MRI. The thalamus is a GM nucleus containing uniformly distributed WM fibers. The mixture of WM and GM gives it very low contrast to the surrounding WM tracks in MRI. However, we can easily identify the boundary between IC and thalamus in OCT. Compared to the PUT, high level of WM in thalamus reduces the optical penetration depth and increases the attenuation coefficient [Fig. 4(d)]. Also, the backscattering intensity from the thalamus is not as high as that from the WM bundles. This result also agrees with a previous study.[14] Figure 4(d) shows that the transitions between PUT and its surrounding tissues are obvious in both imaging modalities, but only OCT provides good contrast between IC and thalamus. Figure 4(f) shows that the attenuation coefficient of thalamus (GM/WM mixture) is between IC (WM) and PUT (GM), and the difference is statistically significant ($P < 0.0001$). The attenuation coefficients in Fig. 4(f) are calculated from 1-cm-wide unsmoothed data at the location indicated by the black arrows in Fig. 4(d). This result suggests that OCT may provide a different contrast to MRI, which could be vital for targeting nuclei in basal ganglia. Contrast in MRI images depends on the magnetic property of the tissue, whereas contrast in OCT lies in light-scattering property. Although the source of the contrast of both imaging modalities comes from two different physical phenomena, OCT is able to produce images at a very high resolution over a small field of view. Such high resolution is currently not possible with MRI. However, these two modalities can complement each other, where MR images may provide guidance to an OCT catheter to a specific location from which high-resolution images may be obtained.

In conclusion, we develop a multiscale MRI/OCT imaging system with tele-operated robot that has potential to improve the accuracy and efficiency of iMRI procedures. Real-time OCT images can fill the gap between pre- and postoperative MRI images and thus allow operators to reach the target more efficiently. Moreover, high-resolution OCT imaging provides microstructural information and different contrast that can be useful for detecting MRI-occult tissue landmarks. Therefore, combining large field-of-view MRI with high-resolution OCT is a promising guidance tool for high-precision surgery. Future work will include the investigation of the impact of physiological motion (breathing, etc.) and biofouling (bleeding, etc.) on targeting accuracy under *in vivo* conditions.

Acknowledgments

This work is supported in part by the UMB-UMCP SEED Grant Program, NIH R21EB012215, R21DK088066, R21AG042700, and NSF CBET-1135514, CBET-1254743.

References

1. W. A. Hall and C. L. Truwit, "Intraoperative MR imaging," *Magn. Reson. Imag. Clin. N. Am.* **13**(3), 533–543 (2005).
2. T. Schulz et al., "Interventional and intraoperative MR: review and update of techniques and clinical experience," *Eur. Radiol.* **14**(12), 2212–2227 (2004).
3. P. S. Larson et al., "An optimized system for interventional magnetic resonance imaging-guided stereotactic surgery: preliminary evaluation of targeting accuracy," *Neurosurgery* **70**(1 Suppl. Operative), 95–103 (2012).
4. G. R. Sutherland, I. Latour, and A. D. Greer, "Integrating an image-guided robot with intraoperative MRI: a review of the design and construction of neuroArm," *IEEE Eng. Med. Biol. Mag.* **27**(3), 59–65 (2008).
5. B. Yang et al., "Design and control of a 1-DOF MRI compatible pneumatically actuated robot with long transmission lines," *IEEE/ASME Trans. Mechatron.* **16**(6), 1040–1048 (2011).
6. N. V. Tsekos et al., "Magnetic resonance-compatible robotic and mechatronics systems for image-guided interventions and rehabilitation: a review study," in *Annual Review of Biomedical Engineering*, pp. 351–387, Annual Reviews, Palo Alto, California (2007).
7. C. P. Liang et al., "A forward-imaging needle-type OCT probe for image guided stereotactic procedures," *Opt. Express* **19**(27), 26283–26294 (2011).
8. A. Ahmad et al., "Cross-correlation-based image acquisition technique for manually-scanned optical coherence tomography," *Opt. Express* **17**(10), 8125–8136 (2009).
9. X. Liu, Y. Huang, and J. U. Kang, "Distortion-free freehand-scanning OCT implemented with real-time scanning speed variance correction," *Opt. Express* **20**(15), 16567–16583 (2012).
10. W. A. Hall and C. L. Truwit, "1.5 T: spectroscopy-supported brain biopsy," *Neurosurg. Clin. N. Am.* **16**(1), 165–172 (2005).
11. E. White et al., "A robust MRI-compatible system to facilitate highly accurate stereotactic administration of therapeutic agents to targets within the brain of a large animal model," *J. Neurosci. Meth.* **195**(1), 78–87 (2011).
12. A. J. Martin et al., "Placement of deep brain stimulator electrodes using real-time high-field interventional magnetic resonance imaging," *Magn. Reson. Med.* **54**(5), 1107–1114 (2005).
13. A. R. Rezai et al., "Deep brain stimulation for Parkinson's disease: surgical issues," *Mov. Disord.* **21**(Suppl. 14), S197–S218 (2006).
14. M. S. Jafri et al., "Optical coherence tomography in the diagnosis and treatment of neurological disorders," *J. Biomed. Opt.* **10**(5), 051603 (2005).
15. M. S. Jafri, R. Tang, and C. M. Tang, "Optical coherence tomography guided neurosurgical procedures in small rodents," *J. Neurosci. Meth.* **176**(2), 85–95 (2009).
16. S. W. Jeon et al., "A feasibility study of optical coherence tomography for guiding deep brain probes," *J. Neurosci. Meth.* **154**(1–2), 96–101 (2006).